Geochemistry, Geophysics, Geosystems

RESEARCH ARTICLE
10.1029/2018GC007944

# New Magnetic Constraints on Early-Middle Miocene Uplift of the Liupan Shan, Northeastern Margin of the Tibetan Plateau

**Jiabin Wu[1,2,3], Licheng Guo[1,2,3], Shangfa Xiong[1,2,3], Shiqi Wang[3,4], Zihua Tang[1,2,3], Chunsheng Jin[1,2], Xiaoxiao Yang[1,2,3], Ning Gu[1,2,3], Chunxiao Li[3,4], and Jingyi Cui[1,2,3]**

[1]Key Laboratory of Cenozoic Geology and Environment, Institute of Geology and Geophysics, Chinese Academy of Sciences, Beijing, China, [2]CAS Center for Excellence in Life and Paleoenvironment, Beijing, China, [3]University of the Chinese Academy of Sciences, Beijing, China, [4]Key Laboratory of Evolutionary Systematics of Vertebrates, Institute of Vertebrate Paleontology and Paleoanthropology, Chinese Academy of Sciences, Beijing, China

**Key Points:**
- A new magnetostratigraphy for the Kaimengou section near the Liupan Shan reveals that it spans the interval from 19.8 to 12.8 Myr
- AMS results show that the Liupan Shan experienced a series of tectonic strain events along an E-W direction during 19.5–14 Myr
- The strain was mainly related to far-field deformation induced by the Indian-Asian collision

**Supporting Information:**
- Supporting Information S1
- Data Set S1
- Data Set S2
- Data Set S3

**Correspondence to:**
J. Wu and S. Xiong,
wujiabin@mail.iggcas.ac.cn;
xiongsf@mail.iggcas.ac.cn

**Citation:**
Wu, J., Guo, L., Xiong, S., Wang, S., Tang, Z., Jin, C., et al. (2019). New magnetic constraints on early-middle Miocene uplift of the Liupan Shan, northeastern margin of the Tibetan Plateau. *Geochemistry, Geophysics, Geosystems*, *20*, 1340–1357. https://doi.org/10.1029/2018GC007944

Received 5 SEP 2018
Accepted 29 JAN 2019
Accepted article online 4 FEB 2019
Published online 7 MAR 2019



**Abstract** New constraints on the uplift history of the Liupan Shan can improve our understanding of the tectonic consequences of the collision of the Indian and Asian plates, including the timing of the uplift of the Tibetan Plateau. Here we present a detailed magnetostratigraphy for the Kaimengou section near the piedmont of the Liupan Shan, which reveals that it spans the interval from 19.8 to 12.8 Myr. Together with the results of measurements of the anisotropy of magnetic susceptibility, rock magnetic measurements show that the anisotropy of magnetic susceptibility is dominated by antiferromagnetic hematite and/or paramagnetic minerals, both of which are mainly controlled by the preferred crystallographic orientation, which can be used to record the tectonic history. During 19.5–14.0 Myr, the maximum principal axis ($K_{max}$) showed a pronounced N-S orientation and $K_{min}$ began to exhibit a girdled distribution in an E-W direction, indicating a slight to moderate tectonic strain in an E-W direction. And the strain can be reconfirmed be the shape parameter ($T$). We attribute the strain to far-field influence by the collision of the Indian and Asian plates. We also present a tentative conceptual model, which explains how the E-W compression fits within the general tectonic scenario for the uplift of the Tibetan Plateau.

## 1. Introduction

The collision of the Indian and Asian plates is one of the most significant tectonic events in the Cenozoic and is closely related to the uplift of the Tibetan Plateau, with major and geographically widespread paleoenvironmental consequences (Fang et al., 2002; Lin et al., 2010; Mulch & Chamberlain, 2006). The northeastern edge of the Tibetan Plateau, including from east to west the Liupan Shan, Haiyuan Fault, Qilian Orogenic Belt, and Altyn Tagh Fault, was substantially influenced by the collision (Figure 1a; Burchfiel et al., 1991; Li et al., 2013; Li et al., 2016; Yan et al., 2006; Zhang et al., 1991). Consequently, detailed knowledge of the uplift of the Liupan Shan is important for understanding the uplift history of the Tibetan Plateau, as well as far-field deformation induced by the collision of the Indian and Asian plates.

A substantial amount of research has focused on the uplift of the Liupan Shan using apatite fission-track (AFT) dating (Gao et al., 2000; Lin et al., 2010; Lin et al., 2011; Zheng et al., 2006), magnetostratigraphy and morphostratigraphy (Liu et al., 2009; Song, Fang, Li, An, & Miao, 2001), Global Positioning System (GPS) measurements (Li et al., 2016; Li, Shan et al., 2017; Wang et al., 2001), electron spin resonance dating (Li et al., 2013), and remote sensing and digital elevation model technology (Shi et al., 2006). Some have argued that mountain uplift began during the Quaternary (Burchfiel et al., 1991; Yang et al., 2002); however, others have proposed that the initiation of uplift occurred at ~8.0 Ma and subsequently intensified at ~5.3 and 3.8 Ma (Ding et al., 2004; Lin et al., 2010; Shen et al., 2001; Song, Fang, Li, An, & Miao, 2001; Song et al., 2005; Song et al., 2000; Song, Fang, Li, An, & Yang, 2001; Zhang et al., 2006; Zheng et al., 2006). Lin et al. (2011) suggested that the far-field influence of the collision of the Indian and Asian plates reached the Liupan Shan during the early Eocene and that this influence was enhanced in the early Miocene, late Miocene, and the Quaternary, which is supported by several other studies (Gao et al., 2000; Liu et al., 2009; Lin et al., 2011; Li et al., 2013). However, the timing of the uplift remains controversial; moreover, most of the current research methods used are more useful for detecting and characterizing major tectonic strain,

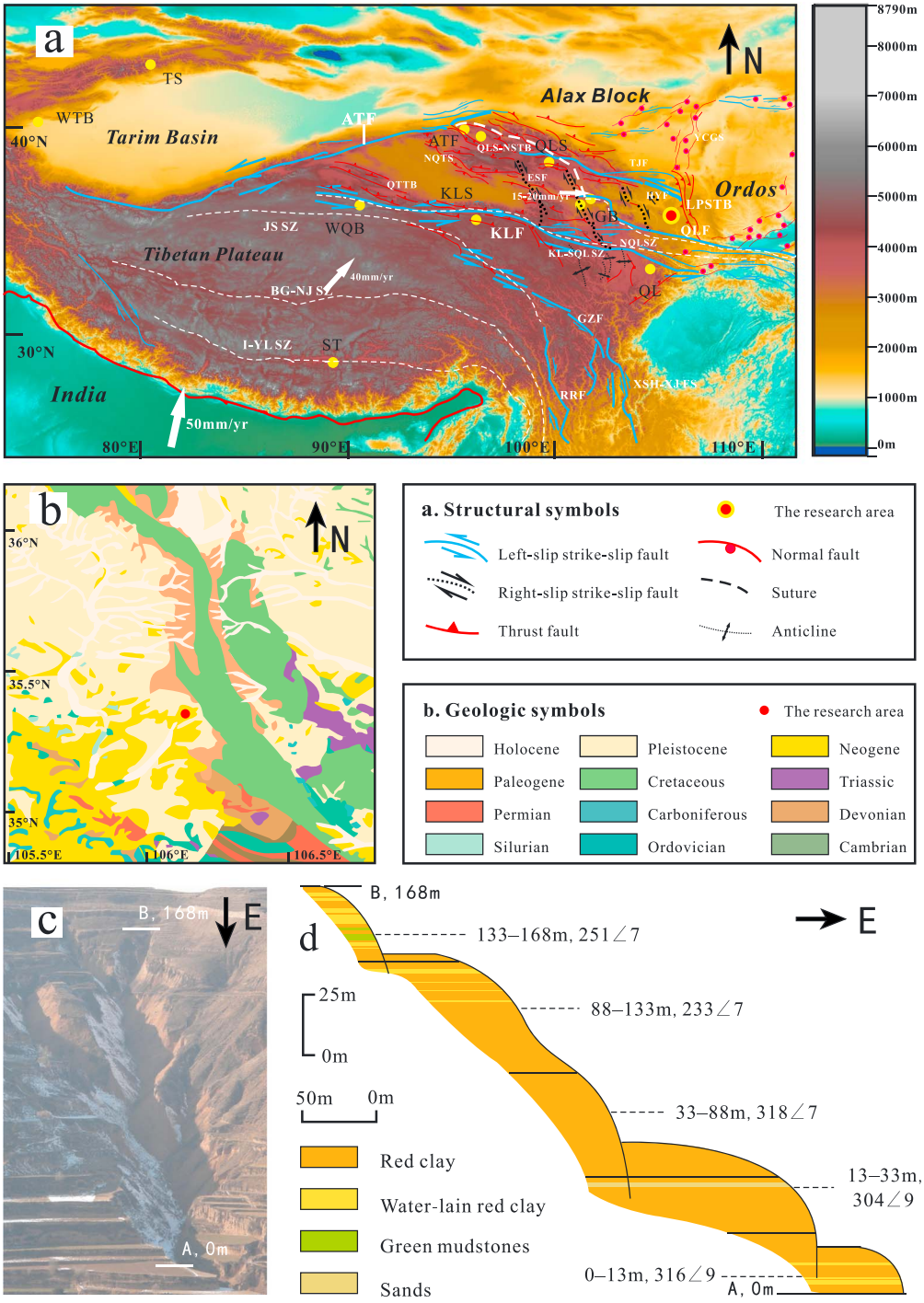


**Figure 1.** (a) Tectonic map of the northeastern margin of Tibetan Plateau, compiled from Burchfiel et al. (1991), Gao et al. (2013), Gaudemer et al. (1995), Taylor and Yin (2009), Yin et al. (2008), and Zuza et al. (2016). The white arrows indicate the movements of the Indian plate, central Tibet, and northeastern-most Tibet, relative to Siberia. The red solid circle is the study area (Kaimengou), in the northeastern margin of the Tibetan Plateau. Left-silp strike-slip fault: ATF, Altyn Tagh fault; TJF, Tianjing fault; KLF, Kunlun fault; HYF, Haiyuan fault; GZF, Ganzi fault; QLF, Qinling fault. RRF, Red River fault; XSH-XJFS, Xiangshuihe-Xiaojiang fault system. Right-silp strike-slip fault: ESF, Elashan fault. Thrust fault: QTTB, Qimen Tagh thrust belt; QLS-NS TB, Qilian Shan-Nan Shan thrust belt; LPSTB, Liupan Shan thrust belt. Normal fault: YCGS, Yinchuan graben system. Suture: I-YL SZ, Indus-Yalu suture zone; BG-NJ SZ, Bangong-Nujiang suture zone; JS SZ, Jinsha suture zone; NQLSZ, North Qinling suture zone; QLS, Qilian suture; KL-SQLSZ, Kunlun-South Qinling suture zone. The yellow solid circles are the study areas, which had done by previous workers. TS, Tian Shan; WTB, The west Tarim basin; ATF, Althn Tagh fault; QLS, Qilian Shan; KLS, Kunlun Shan; GB, Guide Basin; QL, Qin Ling; ST, Southern Tibet. (b) The geologic map of the study area compiled from a public version freely available online. The scale of the map is 1:1000000. The URL is http://ngac.org.cn/Document/Map.aspx?MapId=EC7E1A7A7AD81954E0430100007F182E. The red solid circle indicates the study site. (c) Field photograph of the study area. (d) Geological cross section of the sedimentary sequence.

while weak deformation has been ignored or misinterpreted. Clearly, more evidence is needed, especially of weak tectonic strain.

The anisotropy of magnetic susceptibility (AMS) is valuable for tracing tectonic strain, especially in weakly deformed sediments: it can record the initial deformation and successfully be used in the case of extremely weak strain fields (Cifelli et al., 2009; Larrasoaña et al., 2011; Li, Shan et al., 2017; Parés et al., 1999). The main principles of the use of AMS to characterize tectonic strain can be summarized as follows: (1) In an unstrained environment, the original AMS ellipsoid is characterized by an oblate shape (i.e., $K_{max} \approx K_{int} \gg K_{min}$). The minimum axis of the AMS ellipsoid ($K_{min}$) is perpendicular to the bedding and concentrated in the projection center, while the maximum axis of the AMS ellipsoid ($K_{max}$) is dispersed around the projection plane (Borradaile & Henry, 1997; Lagroix & Banerjee, 2002; Lagroix & Banerjee, 2004). (2) The AMS ellipsoid is transformed from oblate to triaxial (i.e., $K_{max} \approx K_{int} \approx K_{min}$) when it experiences a weak strain. Although $K_{min}$ remains perpendicular to the bedding and is concentrated in the projection center, $K_{max}$ tends to have a clustered distribution perpendicular to the direction of the compression (Larrasoaña et al., 2004; Parés, 2004. (3) As the strain increases, the AMS ellipsoid ultimately becomes prolate (i.e., $K_{max} \gg K_{int} \approx K_{min}$), $K_{min}$ values begin to deviate from the center of the projection plane and spread out along the direction of the strain and $K_{max}$ values become more tightly clustered (Borradaile, 2001; Maffione et al., 2015; Soto et al., 2009; Tang et al., 2012).

Many previous studies have shown that as is the case of Quaternary loess, the pre-Quaternary red clay in the west of the Liupan Shan is mainly of eolian origin and can be traced back to about 25 Ma (Gao et al., 2014; Guo et al., 2002; Qiang et al., 2011; Sun et al., 2010; Zhang et al., 2011). Thus, the red clay is an important source of information for reconstructing the uplift of the Liupan Shan since the Miocene. Here we present the results of a detailed study of the magnetostratigraphy and magnetic fabric of the Kaimengou section, in Zhuanglang County, which we use to reconstruct the uplift history of the Liupan Shan and to further consider the far-reaching influence of the collision of the Indian and Asian plates.

## 2. Geological Setting

The Liupan Shan is a north-south trending mountain range located in the central Chinese Loess Plateau and divides the plateau into two parts; thus, the Liupan Shan is a major geological and geographical boundary (Ao et al., 2016). In terms of the tectonic configuration of the region, the Ordos Block is in the east, the Longzhong Basin is in the west, the Qilian-Haiyuan Fold Belt is in the north, and the Qinling Fold Belt is in the south (Figure 1a). The Liupan Shan is connected to the Haiyuan Fault and the Qilian Orogenic Belt, and finally, it is in conjunction with the Altyn Fault; it is regarded as the northeasternmost boundary of the Tibetan Plateau (Figure 1a; Li et al., 2013; Li, Shan et al. (2017); Song, Fang, Li, An, & Miao, 2001; Song et al., 2005; Zheng et al., 2006).

The Kaimengou section (106.13°E, 35.37°N) is in Liufang village, Zhuanglang County, Gansu Province. It is located near the piedmont of the Liupan Shan, at an altitude of 1,840 m, and is strongly influenced by the adjacent mountains; hence, the red clay deposits of the area are well suited to reconstruct the tectonic strain history. The red clay sequence is ~168 m thick, and it does not reach bedrock at the base. As is the case of other red clay sections, the sediments are of primary eolian origin, with water-lain red clay confined to the base and top of the section. The section can be divided into five intervals, as follows (Figure 2): (i) 153–168 m: Water-lain red clay with horizontal laminations, alternating with typical unstratified eolian red clay. (ii) 145–153 m: This interval contains two distinct green layers, mainly grayish-green mudstone, with obvious interbedded disturbed layers, interpreted as bog facies. Within these layers numerous mammal fossils have been discovered, which were identified by Shiqi Wang (Institute of Vertebrate Paleontology and Paleoanthropology, Chinese Academy of Sciences). They include *Turcocerus* sp. (Deng et al., 2013), rhinoceros, elephant, and several ruminants. And Deng et al. (2013) found that *Turcocerus* sp. first appeared in the fossil record at ~16.2 Ma and disappeared at about ~11.6 Ma can be used as a tie point for the correlations between the polarity sequence in our section and the geomagnetic polarity timescale (GPTS; Ogg et al., 2016). (iii) 123–145 m: This interval is dominated by eolian deposits, which are occasionally interbedded with minor amounts of water-lain red clay. (iv) 8–123 m: Typical eolian red clay, with no horizontal bedding and with no evidence of fluvial influences; a sand layer occurs at 45 m. (v) 0–8 m: The basal part of the section consists of fluvially reworked red clay layers alternating with typical eolian red clay.

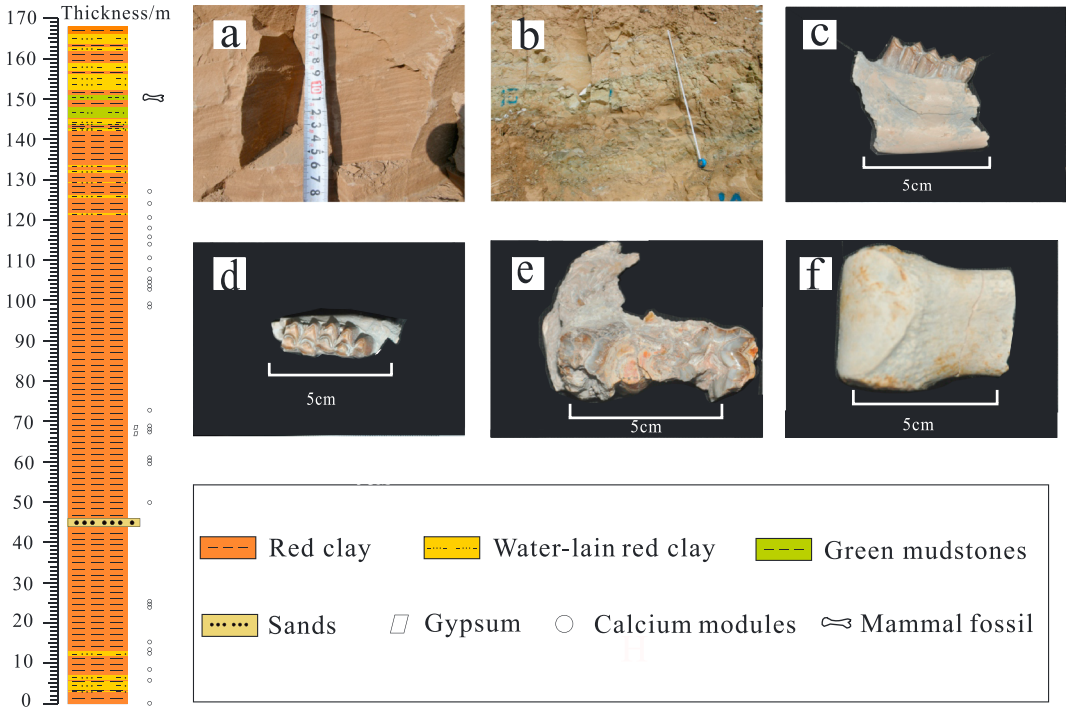


**Figure 2.** Lithology column for the Kaimengou section and photographs of major lithologies and fossil discoveries. The red clay sequence is 168 m thick. The sediments of the entire section are of primary eolian origin; however, water-lain red clay occurs at the top and bottom of the section. (a) Water-lain red clay with horizontal laminations. (b) Predominantly grayish-green mudstone with distinct interbedded disturbed layers, which may be bog facies. (c) Inferior cheek teeth of *Turcocerus* sp. (lateral view). (d) Inferior cheek teeth of *Turcocerus* sp. (crown view). (e) elephant. (f) rhinoceros.

## 3. Materials and Methods

Depending on the sediment outcrop quality, samples were collected as oriented hand samples, and we collected 1,680 oriented block samples at a 10-cm interval throughout the entire section. Each oriented hand sample was cut into four cubic (2-cm edge) specimens. The specimens were transported to and analyzed at the Paleomagnetism and Geochronology Laboratory of the Institute of Geology and Geophysics, Chinese Academy of Sciences.

### 3.1. Rock Magnetic Properties

To determine the main magnetic carrier minerals, six representative samples were selected for measurements of temperature-dependent magnetic susceptibility ($\chi$-$T$), hysteresis loops, and acquisition and backfield demagnetization of isothermal remanent magnetization (IRM). $\chi$-$T$ curves were measured with an AGICO KLY-4 Kappabridge in a magnetic field of 200 A/m, at a frequency of 976 Hz; the heating rate was ~12 °C/min. To prevent oxidation of the samples, the measurements were conducted in an argon atmosphere. Hysteresis loops and acquisition/demagnetization of IRM were measured with a vibrating sample magnetometer (Princeton Measurements, MicroMag 3900), with a sensitivity of $5 \times 10^{-10}$ $Am^2$. Magnetizations were imparted and demagnetized within the field range of ±1.5 T.

### 3.2. Thermal Demagnetization of Natural Remanent Magnetization

Initially, we selected 840 specimens at an interval of 20 cm for natural remanent magnetization (NRM) demagnetization experiments, and subsequently, we increased the number of samples for the intervals in which magnetic polarity reversals were more frequent. A total of 1,057 specimens were measured. Stepwise thermal demagnetization of the NRM was conducted using an ASC TD-48 thermal demagnetizer, with a residual field of <30 nT. Remanences were measured with a 2G Enterprises 760 three-axis cryogenic magnetometer. Both the demagnetizer and the magnetometer were housed in a magnetically shielded space (<300 nT). The heating steps used for thermal demagnetization of the NRM comprised 23 steps, from 25 to 680 °C, with increments ranging from 10 to 55 °C. All the evaluations were processed using the PaleoMag software developed by Craig H. Jones and Joya Tetreault.

### 3.3. Anisotropy of Magnetic Susceptibility

The AMS of all 1057 oriented specimens were measured using an AGICO KLY-3S Kappabridge susceptibility meter (AGICO Inc.) with an internal magnetic field strength of 300 A/m with a frequency of 976 Hz and a sensitivity of $2.0 \times 10^{-8}$ SI. All the evaluations and plots were produced with Stereonet 10.0 software developed by Nestor Cardozo and Richard Allmendinger.

## 4. Results

### 4.1. Rock Magnetism

#### 4.1.1. Temperature Dependence of Magnetic Susceptibility

The temperature dependence of magnetic susceptibility ($\chi$-$T$ curves) is useful for determining the magnetic mineralogy of specimens (Dunlop & Ozdemir, 2001; Tang et al., 2012; Tang et al., 2015). The heating curves (Figure 3a) show a steady increase in susceptibility at temperatures below 300 °C, which may indicate the presence of ferrimagnetic grains with sizes near the superparamagnetic/single domain boundary, and which are gradually unblocked during the heating process (Deng et al., 2006; Zhao et al., 2017). A decrease in magnetic susceptibility occurs within the temperature interval of 300–450 °C, which results from the conversion of maghemite to hematite ($\gamma Fe_2O_3 \rightarrow \alpha Fe_2O_3$; Li, Ma et al., 2017; Sun et al., 2011). The heating curves of the samples from the depths of 167.7, 130.3, and 22.1 m show a hump between 500 and 520 °C, which may reflect the neoformation of strongly magnetic minerals, or the Hopkinson effect for single domain magnetite (single domain and/or quasi-single domain magnetite; Deng, 2008; Deng et al., 2002; Li, Ma et al., 2017). All the curves show a sharp decrease near 580 °C, the Curie temperature of magnetite, indicating that magnetite dominates the magnetic susceptibility (Li, Yue et al., 2014; Li, Ma et al., 2017; Zhao et al., 2017). In addition, there is a minor final decay of the magnetic susceptibility in the heating curves above 585 °C, suggesting the presence of hematite (Tang et al., 2015). In the cooling curves, the magnetic susceptibility of all the samples is substantially higher, indicating the neoformation of magnetite during heating (Li, Yue et al., 2014).

#### 4.1.2. IRM Acquisition Curves

To further characterize the magnetic mineralogy of the samples, especially the high-coercivity component, IRM acquisition curves of six typical samples were measured (Figure 3b; Ge et al., 2014; Xiong et al., 2017). All the samples acquired more than 75% of their $IRM_{1.5T}$ intensity at 0.3 T, and all the remanent magnetization was removed after exposure to reversed fields of <60 nT, indicating the dominance of low-coercivity minerals. However, the remanence remained unsaturated even in fields up to the initial saturating field, indicating the presence of high-coercivity minerals (Li, Ma et al., 2017; Sun et al., 2011; Tang et al., 2015).

#### 4.1.3. Hysteresis Loops

Hysteresis loops provide information about the type and domain state of magnetic minerals (Figure 3c; Xiong et al., 2017). The magnetization of all the six selected samples reached more than 84% of the saturation magnetization at 0.3 T, confirming the dominance of low-coercivity minerals; however, the loops remained open even at 1 T, again confirming the presence of a high-coercivity component. In addition, the loops are all wasp-waisted (narrow in the center and wider above and below), indicating the coexistence of both low- and high-coercivity minerals (Ge et al., 2014; Li, Yue et al., 2014; Li, Ma et al., 2017; Sun et al., 2011; Tang et al., 2015).

### 4.2. Thermal Demagnetization of NRM

The thermal demagnetization results were analyzed by principal components analyses (Kirschvink, 1980), and we ensured that a minimum of four consecutive demagnetization steps above 400 °C (typically 7–10) were used to determine the characteristic remanent magnetization (ChRM) direction. The maximum angular deviation was less than 15° (for 80% of the samples, less than 10°). A total of 796 samples out of the original 1057 (75%) yielded stable ChRM directions. The demagnetization results of representative samples are illustrated using orthogonal diagrams (Figure 4; Zijderveld, 1967). The viscous component of magnetization was removed at temperatures up to 350 °C. The results in Figures 4c–4e show that as the temperature approached 580 °C, the remanence was reduced by >90%, indicating that magnetite is the dominant carrier of the ChRM. However, Figures 4a, 4b, 4c, and 4f show that the remanence was not removed completely, even at 680 °C. Nevertheless, there were no changes in the magnetization direction at temperatures above and below 580 °C, suggesting that both magnetite and hematite are the carriers of the ChRM, with both having the same ChRM direction.

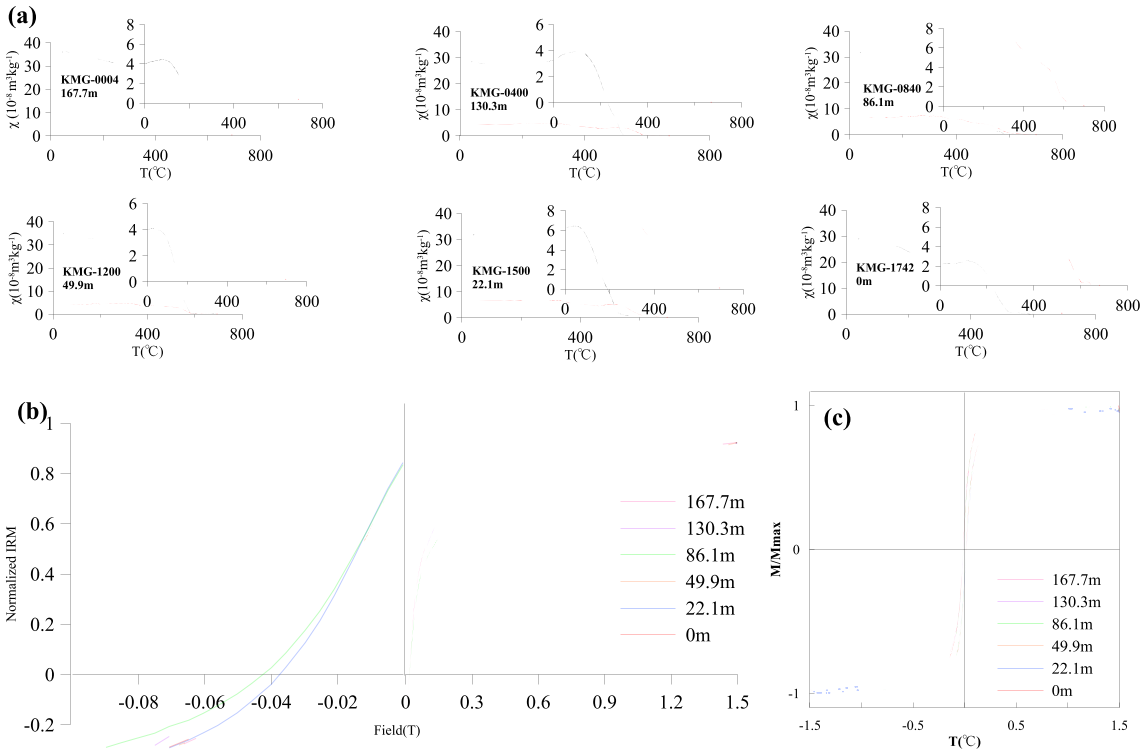


**Figure 3.** (a) Low-field temperature dependence of magnetic susceptibility ($\chi$-$T$) for selected samples. (b) Isothermal remanent magnetization acquisition curves for selected samples. (c) Hysteresis loops for selected samples.

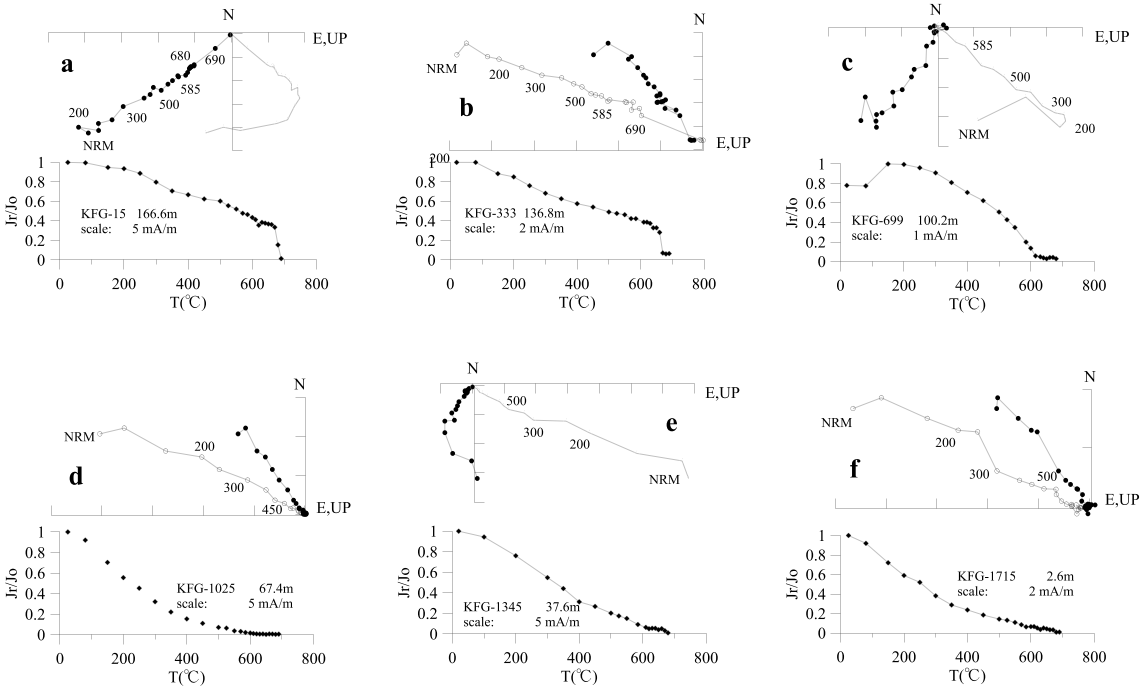


**Figure 4.** Demagnetization of the stepwise thermal demagnetization (in stratigraphic coordinates) plotted on orthogonal diagrams and the decay of the remanent magnetization. In the orthogonal diagrams, the solid (open) squares represent declination (inclination) values at each step.

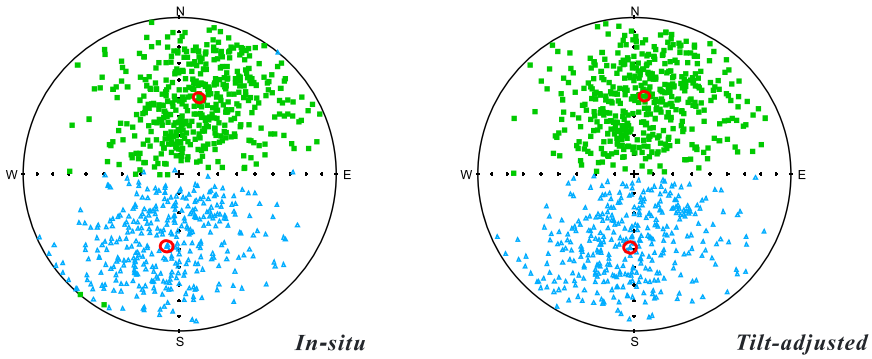


| Thickness interval/m | Age interval /Ma | Dip/dip angle | n | N/R | $D_N/D_R$ | $I_N/I_R$ | $\kappa_N/\kappa_R$ | $\alpha_{95N}/\alpha_{95R}$ |
|---|---|---|---|---|---|---|---|---|
| 133-168 | 12.8-14.1 | 251/7 | 170 | 112/58 | 26.1/177.1 | 41.5/-56.6 | 7/6.5 | 6.8/9.9 |
| 88-133 | 14.1-16.7 | 233/7 | 235 | 114/121 | 11.7/189.7 | 53.6/-50 | 9.3/7.2 | 5.7/6.4 |
| 33-88 | 16.7-18.0 | 318/8 | 227 | 77/150 | 338.8/178.4 | 57.6/-49.8 | 11.1/7.3 | 6.3/5.7 |
| 13-33 | 18.0-19..3 | 304/9 | 94 | 78/16 | 2.1/198.1 | 45.4/-36.9 | 10.1/9.6 | 6.6/16 |
| 0-13 | 19.3-19.8 | 316/7 | 70 | 62/8 | 3.4/190.2 | 35/-56.6 | 11.8/9.8 | 6.8/22.9 |
| 0-168 | 12.8-19.8 | | 796 | 443/353 | 7.8/183.6 | 48.2/-50.7 | 7.7/7.1 | 3.2/3.8 |

**Figure 5.** Equal area stereographic projections of the characteristic remanent magnetization directions of the 796 samples from the Kaimengou section, shown in geographic (in situ) and stratigraphic (tilt-corrected) coordinates. The green squares and the blue triangles represent normal and reversed inclinations, respectively. The red circles represent the mean direction of the normal and reversed polarity components. The results pass a class C reversal test at 95% confidence, using the PaleoMag software developed by Craig H. Jones and Joya Tetreault (McFadden & McElhinny, 1990). The table was the mean directions of characteristic remanent magnetization (tilt-corrected).

Before tilt correction, the mean normal and reversed polarity directions are $D_N = 14.4°$, $I_N = 48.4°$ ($N_N = 444$, $\kappa_N = 7.1$, $\alpha_{95N} = 2.7$), and $D_R = 190°$, $I_R = -51.2°$ ($N_R = 352$, $\kappa_R = 6.8$, $\alpha_{95R} = 3.1$), respectively. After tilt correction, $D_N = 7.5°$, $I_N = 48.5°$ ($N_N = 444$, $\kappa_N = 7.6$, $\alpha_{95N} = 2.6$), and $D_R = 183.1°$, $I_R = -51.1°$ ($N_R = 352$, $\kappa_R = 6.8$, $\alpha_{95R} = 3.1$). The mean tilt-corrected inclination (50°) is within 5° of the mean inclination expected for the sample location, indicating only a minor inclination error (Besse & Courtillot, 2003). In addition, the results pass a class C reversals test, using the PaleoMag software developed by Craig H. Jones and Joya Tetreault (Figure 5; McFadden & McElhinny, 1990). Virtual geomagnetic pole latitudes were calculated from the ChRM vector parameters (declination $D$ and inclination $I$) and the latitude and longitude of the sampling location (Tauxe et al., 2010). After constructing the magnetic polarity sequence from the virtual geomagnetic pole latitudes (Figure 6), a total of 16 normal and 17 reversed polarity zones were identified. The magnetostratigraphy was provisionally assessed using the magnetic susceptibility results of Guo et al. (2002) for the Qin'an sequence and the mammalian fossil assemblage (*Turcocerus* sp.) within the first green layer from the study section, which is dated to 16.2–11.6 Myr (Deng et al., 2013). Then, two possible correlations to the GPTS (our preferred correlation versus an alternative; Figure 7) have been proposed. Comparison of the two correlations. The alternative indicates an extremely high deposition rate from 73 to 88 m, and it is not well correlated with C5Dr.1n. Our preferred chronology is more reasonable, and with this correlation the mean sediment accumulation rate is 2.43 cm/kyr, which is consistent with the results of Guo et al. (2002) for the Qin'an section (1.6 cm/kyr) and with those of Qiang et al. (2011) for the Zhuanglang section (2.9 cm/kyr). The magnetostratigraphy is well correlated with the GPTS (Ogg et al., 2016) from C5Ar.3r–C6r (Figure 6). Based on the correlation with the GPTS and extrapolation of the sediment accumulation rate, the ages of the top and bottom of the profile are 12.8 and 19.8 Ma, respectively.

### 4.3. Anisotropy of Magnetic Susceptibility

Stereographic projections of the AMS principal axes in geographic and in stratigraphic coordinates are illustrated in Figure 8. The tilt-corrected maximum susceptibility axis ($K_{max}$) directions are clustered in the N-S direction, and the $K_{min}$ directions are distributed in an E-W direction.

In contrast to the ChRM characteristics, the AMS of the section is dominated by anisotropic antiferromagnetic hematite and/or paramagnetic clays. The reasons for this conclusion are as follows: (1) The SIRM ranges from 1.5 to 2.9 $\times 10^{-3}$Am$^2$/kg (Figure 8c), which suggests that the concentration of magnetite can be ignored (Hrouda & Kahan, 1991; Tang et al., 2012); (2) the value of $K_m$ is independent with the $P_j$, indicating that the AMS of the section is not dominated by anisotropic magnetite (Figure 8d); and (3) the

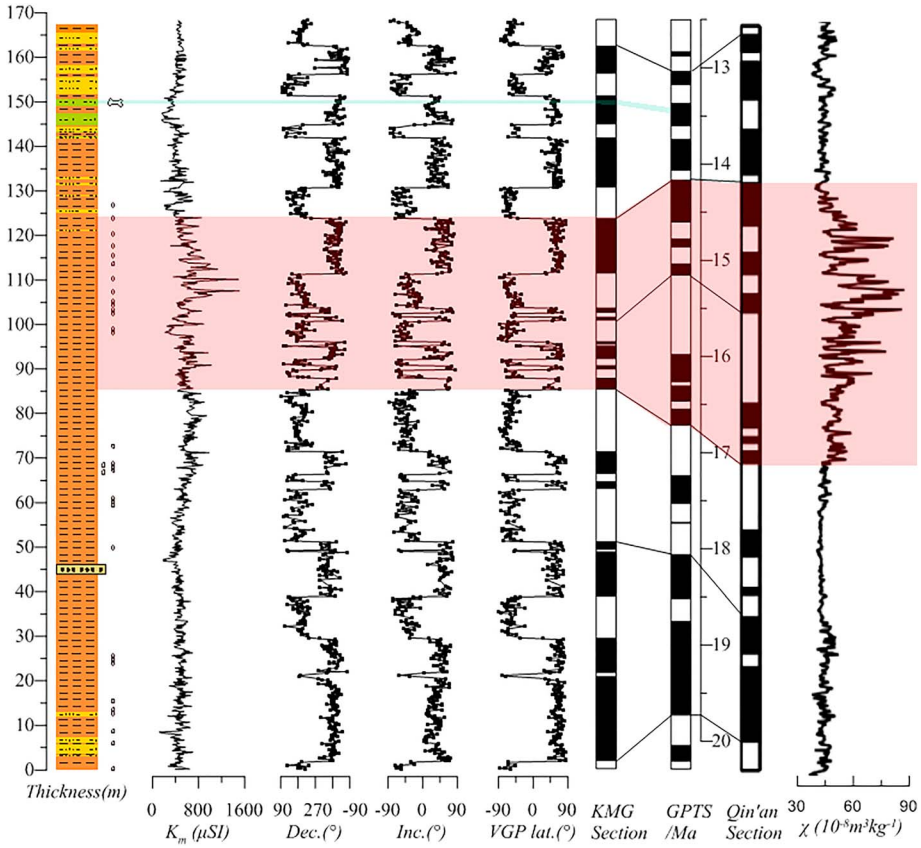


**Figure 6.** (left column) Lithology, bulk magnetic susceptibility, and magnetostratigraphy of the Kaimengou section; (middle column) geomagnetic polarity timescale (GPTS; Ogg et al., 2016); and (right column) magnetostratigraphy and bulk magnetic susceptibility of the Qin'an section (Guo et al., 2002). Fossils of *Turcocerus* sp. were discovered in the green layer (blue shaded layer in Figure 6), indicating an age of 16.2–11.6 Myr (Deng et al., 2013). The bulk magnetic susceptibility record of the Kaimengou section is well correlated with that of the Qin'an section (the pink shaded layer), and the magnetostratigraphy is well correlated with the GPTS from C5Ar.3r–C6r (Ogg et al., 2016). The estimated ages of the top and bottom of the profile are 12.8 and 19.8 Ma, respectively.

volume susceptibility record (Figure 9) indicates a minor ferromagnetic contribution to the bulk susceptibility (<0.1%; Hrouda & Kahan, 1991; Huang et al., 2006; Lu, Wang, & Meng, 2014). These characteristics indicate that the AMS is dominated by anisotropic hematite and/or clay minerals, the preferred crystallographic orientation of which can be used to record the tectonic history (Borradaile & Henry, 1997; Parés, 2004).

Lithostratigraphy, bulk magnetic susceptibility ($K_m$), the median diameter (*D50*), corrected anisotropy degree ($P_j$), the shape parameter ($T$), and the inclinations of the minimum principal axis of the AMS ellipsoids (Inc-$K_{min}$), and the magnetostratigraphic results for the study section are shown in Figure 9. The bulk susceptibility ranges from 94 to 1,207 μSI with an average of 412 μSI. Based on the changes in the shape of the AMS ellipsoid and the $K_{min}$ inclination, the section can be divided into five intervals (Figure 9). In intervals (i) and (v) (with yellow shadow), almost all the values of the shape parameter ($T$) are >0° and the inclinations of the minimum principal axis of the AMS ellipsoids (Inc-$K_{min}$) are >70°. In intervals (ii), (iii), and (iv) (with blue and purple shadow), the shape parameter ($T$) is <0°, and some values of Inc-$K_{min}$ are <70°, especially in intervals (ii) and (iv) (with purple shadow). These features will be discussed in detail in section 5.2.

## 5. Discussion

### 5.1. Interpretation for the AMS Fabrics

At first sight in Figure 9, it appears that the changes in the AMS fabrics are related to lithology. This is because more prolate AMS fabrics, with deviated $K_{min}$ directions, appear to be very well correlated with

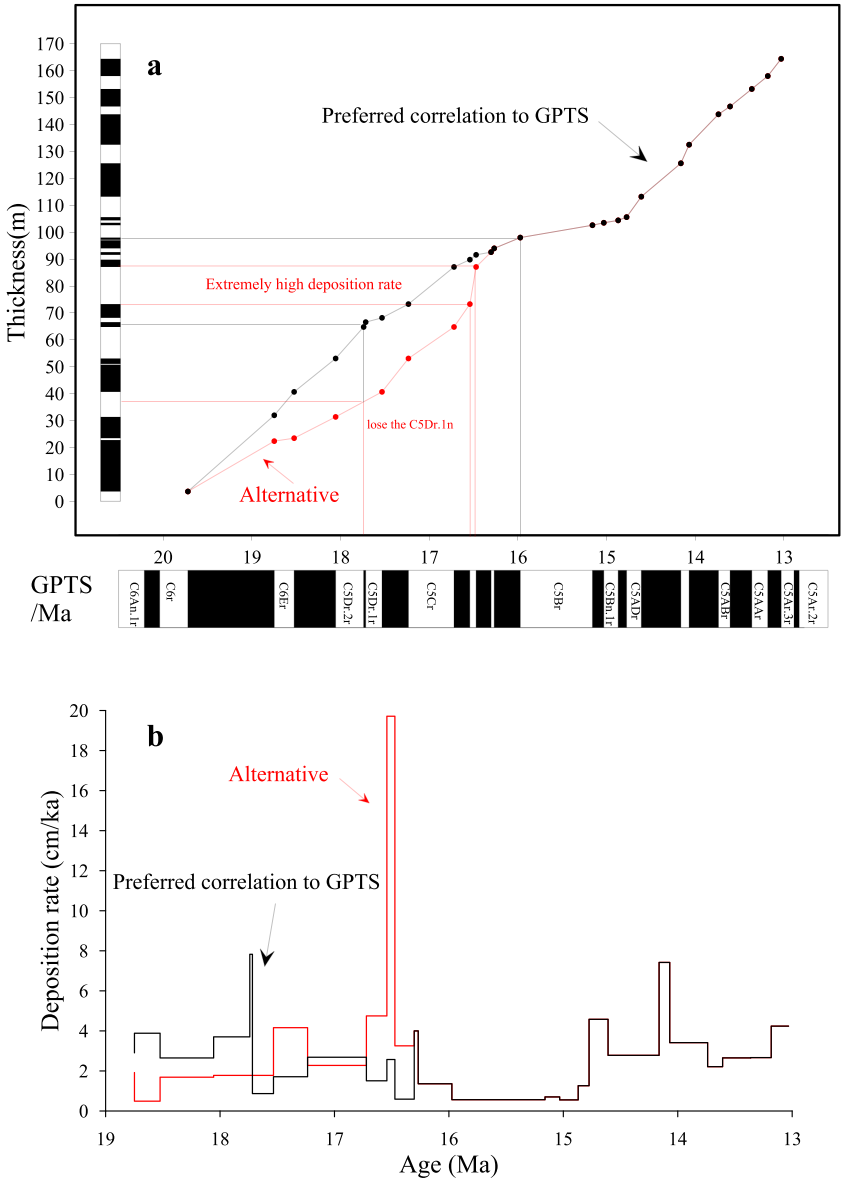


**Figure 7.** Comparison of two possible correlations to the geomagnetic polarity timescale (GPTS; Ogg et al., 2016; our preferred correlation versus an alternative correlation). (a) Present-day stratigraphic thickness versus age. (b) Sediment-accumulation rates (using present-day thicknesses) versus age. The alternative correlation indicates an extremely high deposition rate from 73 to 88 m, and it is not well correlated with C5Dr.1n. With our preferred correlation, the mean sediment accumulation rate is 2.43 cm/kyr, which is consistent with the results of Guo et al. (2002) for the Qin'an section (1.6 cm/kyr) and with those of Qiang et al. (2011) for the Zhuanglang section (2.9 cm/kyr).

the occurrence of primary eolian sediments. However, this is refuted by the following points. (i) In Figure 9, the pattern of more oblate AMS fabrics, with original $K_{min}$ directions, within intervals of water-lain sediments, is not applicable to the whole section; an example is the interval from 135 to 145 m, which is dominated by eolian deposits, if the AMS fabrics are controlled by changes in lithology, the magnetic susceptibility ellipsoid should be prolate, with $K_{min}$ beginning to deviate from the bedding, but this is contrary to what is observed. In addition, the pattern is not applicable to the interval from 7 to 12 m. (ii) Although the magnetic anisotropy can be influenced by the depositional regime, the increase in slope or current can lead to an offset of the $K_{min}$ axes from vertical (Antoine et al., 2014; Taylor & Lagroix, 2015). But combine with the shape parameter ($T$) in Figure 9. During the interval from 18.5 to 14 Myr, the shape parameter ($T$) is <0°, indicating the AMS ellipsoid becomes

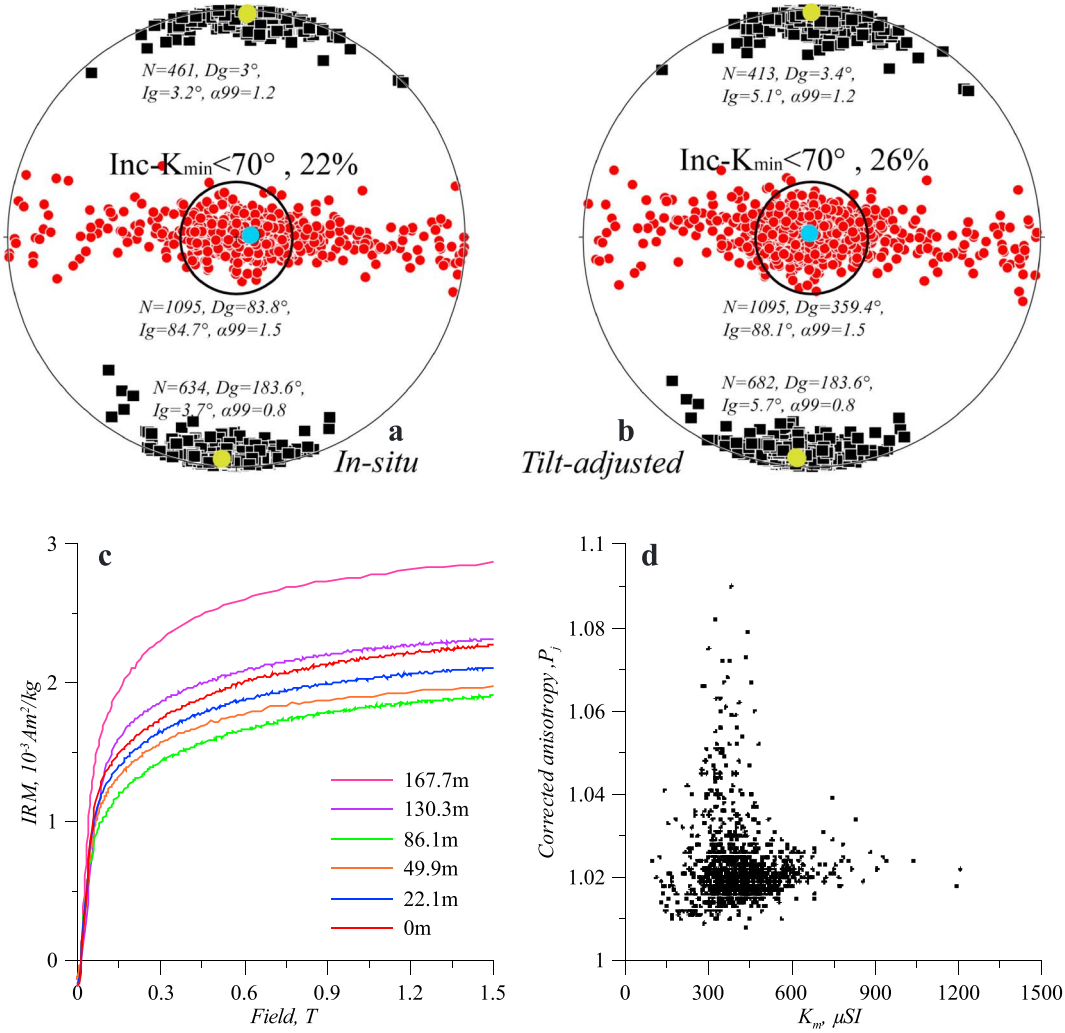


**Figure 8.** Stereographic projections of the anisotropy of magnetic susceptibility principal axes, including maximum ($K_{max}$) and minimum ($K_{min}$) directions in (a) geographic and (b) stratigraphic coordinates. The black boxes and the red circles represent the $K_{max}$ and $K_{min}$ axes, and the green and blue solid circles represent their respective mean values. The black circles show the number of samples whose inclinations of the minimum principal axis is <70° (the percentage of the samples in which $K_{min}$ deviated from the bedding plane). (c) Isothermal remanent magnetization acquisition curves for selected samples shown in Figure 3. (d) Mean magnetic susceptibility ($K_m$) versus corrected anisotropy ($P_j$).

prolate, a strain happened during the interval (Parés, 2004). It is the strain not lithology causing the changes in the AMS fabrics during this period. (iii) Although there are some water lain red clay confined to the base and top of the section, the changes in the lithology within the section are very small (see *D50* in Figure 9).

In the red clay sediments of the Chinese Loess Plateau, it is evident that the AMS orientation can be influenced by wind direction (Gong et al., 2015; Thistlewood & Sun, 1991; Zhang et al., 2010). In Figure 8, the direction of the $K_{max}$ may indicate that a north-south wind (the winter monsoon) played a major role in the air circulation during early-middle Miocene. What is more, the distribution of $K_{max}$ may become more tightly clustered, reinforced by a tectonic strain in W-E direction.

However, the shape parameter ($T$) in Figure 9 shows that almost all the AMS ellipsoid has become prolate ($T < 0°$) during the interval from 18.5 to 14 Myr; we can confirm a strain was happening here (Parés, 2004). The strain can be reconfirmed by the distribution of $K_{min}$ (Figure 8). And the observed pattern (The observed $K_{max}$ direction is near N-S, and partial $K_{min}$ deviated from the center with a girdle

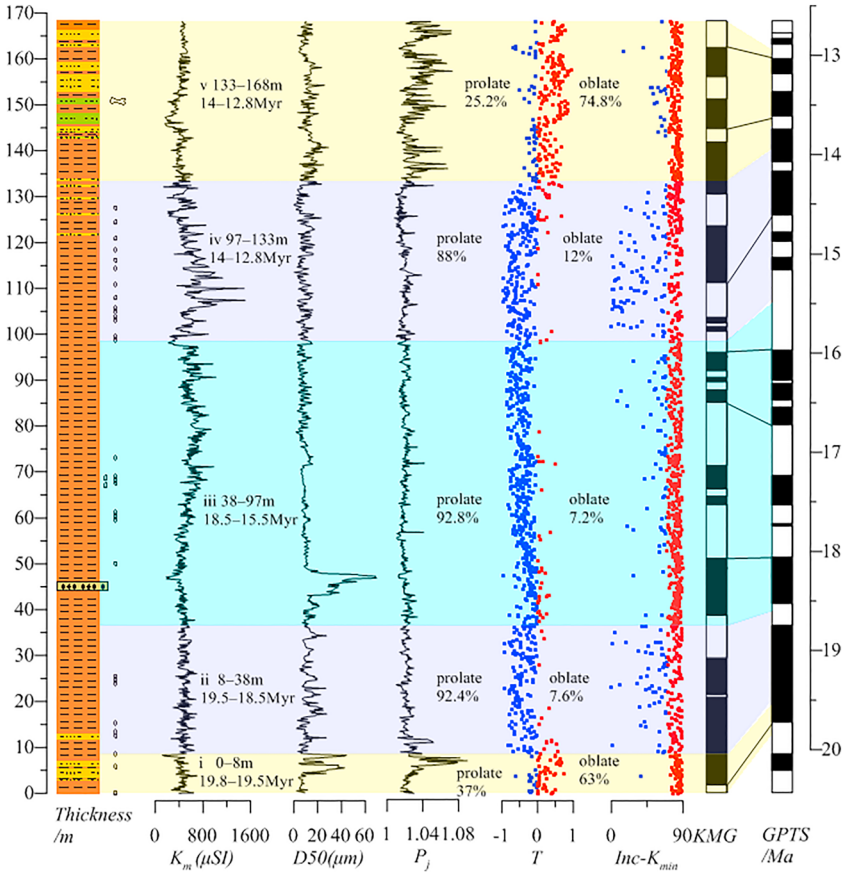


**Figure 9.** From left to right: Lithostratigraphy, bulk magnetic susceptibility ($K_m$), the median diameter ($D50$), corrected anisotropy degree ($P_j$), shape parameter ($T$), the inclinations of the minimum principal axis of the AMS ellipsoids (Inc-$K_{min}$), and the magnetostratigraphy of the Kaimengou section. Based on the changes in the shape of the anisotropy of magnetic susceptibility ellipsoid and the $K_{min}$ inclination, the section can be divided into five intervals, which are indicated by different colors.

distribution in the E-W direction) is interpreted as a slight to moderate tectonic strain overprint on the original sedimentary fabric, with the main direction being E-W (Lu, Wang, & Meng, 2014; Tang et al., 2015). And for the strain is just in a slight to moderate stage, the intensity is not strong enough to transform the magnetic fabric after the diagenetic processes have ended (Huang et al., 2006; Parés, 2004). Thus, we interpret our AMS records as a sensitive proxy for tectonic strain. Numerous studies have also speculated that the magnetic fabric is a sensitive proxy, which begins to develop after deposition and development ceases when diagenetic processes have ended (Burmeister et al., 2009; Cifelli et al., 2004; García-Lasanta et al., 2018; García-Lasantaa et al., 2013).

From the foregoing, we can infer that the changes in the AMS fabrics are effected by both of the winter monsoon and strain. The palaeowind here during early-middle Miocene was in a north-south direction. And during the interval from 18.5 to 14 Myr, a strain was really happening here with a E-W direction in a slight to moderate stage. To further investigate the changes in strain intensity, the profile is divided into five intervals, as follows (Figures 9 and 10):

### 5.2. Evolution of Tectonic Strain in the Liupan Shan

Based on the changes in strain intensity, the profile can be divided into five intervals, as follows (Figures 9, 10):

Interval (i) (0–8 m, 19.8–19.5 Myr; with yellow shadow): The $K_{min}$ axes are almost perpendicular to the bedding (Inc-$K_{min}$ > 70° in almost all cases), which is characteristic of a primary sedimentary fabric, and

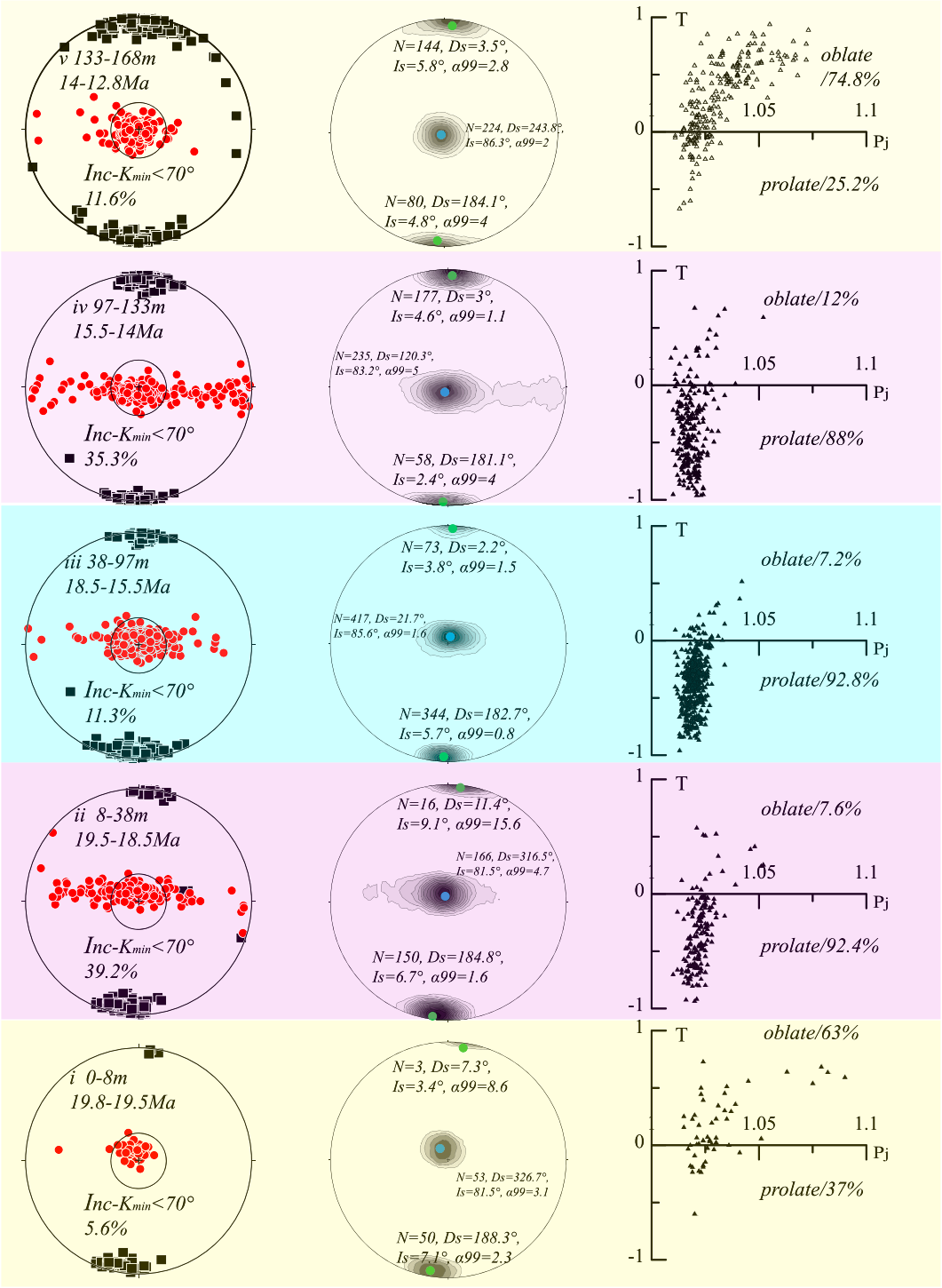


**Figure 10.** Stereographic projections of the anisotropy of magnetic susceptibility (AMS) principal axes, including maximum ($K_{max}$) and minimum ($K_{min}$) directions in stratigraphic coordinates, and the $P_j$-$T$ diagram (corrected AMS degree versus AMS shape parameter) for the five intervals of the section defined by changes in inferred strain intensity.

the strain does not the main cause for the change in the AMS. The direction of the $K_{max}$ indicate a north-south wind (the winter monsoon) played a major role in the air circulation during early-middle Miocene. What is more, the $P_j$-$T$ diagram shows that the shape of the AMS ellipsoid of a substantial number of samples (almost 37%) has changed from oblate ($T > 0$) to prolate ($T < 0$), indicating that

an initial minor deformation occurred during this interval (Huang et al., 2006; Lu, Wang, & Meng, 2014). The distribution of $K_{max}$ may become more tightly clustered for weak tectonic strain in W-E direction.

Interval (ii) (8–38 m, 19.5–18.5 Myr; with purple shadow): Although the majority of the $K_{min}$ axes are still perpendicular to the bedding, a substantial proportion (39.2%) deviate, with an E-W-oriented distribution, indicating that the strain was increased during this interval. This inference is confirmed by the $P_j$-$T$ diagram, which shows that a high proportion of samples (92.4%) have switched from oblate ($T > 0$) to prolate ($T < 0$). We conclude that the red clay in this interval was subjected to intermediate deformation.

Interval (iii) (38–97 m, 18.5–15.5 Myr; with blue shadow): A large proportion of the $K_{min}$ axes are perpendicular to the bedding, but some have deviated. However, compared with interval (ii), the number of samples deviating from the center is much less (11.3%), indicating that the strain decreased during this interval. nevertheless, the strain was still substantial compared to that in interval (i), and the proportion of prolate AMS ellipsoids is 92.8%. We conclude that this interval was subjected to minor deformation.

Interval (iv) (97–133 m, 15.5–14 Myr; with purple shadow): A large proportion of the $K_{min}$ axes deviate from the bedding plane (35.3%) and the densest distribution of $K_{max}$ values is in the N-S girdle, indicating greater strain compared to interval (iii), which is confirmed by the $P_j$-$T$ diagram. We conclude that this interval experienced intermediate deformation.

Interval (v) (133–168 m, 14–12.8 Myr; with yellow shadow): As in interval (i), almost all the $K_{min}$ axes are perpendicular to the bedding, and the $K_{max}$ values are distributed within a N-S direction; the proportion of prolate AMS ellipsoids is 25.2%, indicating that the north-south wind (the winter monsoon) is the main cause for the change in the AMS. And the direction of the $K_{max}$ may be reinforced by a very weak tectonic strain in W-E direction.

### 5.3. Interpretation of the Evolution of Tectonic Strain Affecting the Kaimengou Section

The AMS results show that the Liupan Shan experienced a series of tectonic strain events along an E-W direction during 19.5–14 Myr. Combined with the results of previous research, we conclude that uplift in the Liupan Shan area was closely related to the collision of the Indian and Asian plates (Li et al., 2016; Li, Shan et al., 2017; Lin et al., 2010; Song et al., 2005; Wang et al., 2001; Zheng et al., 2006). The northward movement of the Indian Plate caused the progressive uplift of the Tibetan Plateau (Figure 11a). When the Tibetan Plateau was uplifted to a specific degree, the gravity effect combine with the northward push from Indian plate, part of the plateau block migrated northward towards the Asian plate; then a series of mountains such as Qin Lin, Kunlun Shan, Qilian Shan, and Tian Shan uplifted, which leaded to the topography of the East West high low in China. Under the gravity effect (from the West to the East) and the far-field influence of the collision of the plates, the plateau block escaped eastward via the Altyn Fault Zone, the East Kunlun Fault Zone, and the Liupan Shan Fault. Subsequently, the motion of the plateau block was terminated by the eastern Ordos Block, and the resulting collision and crustal extrusion resulted in the uplift of the Liupan Shan. This tectonic escape scenario, controlled by the collision of the Indian and Asian plates, has been simulated using physical modeling (Tapponnier et al., 2001; Tapponnier & Molnar, 1976). In addition, the distribution of the compressive strain field in the region has been verified by GPS observations (Figure 11c; Wang et al., 2001; Yan et al., 2006).

A conceptual model is shown in Figure 11, which illustrates the timing differences between the uplift of the Tibetan Plateau, the Liupan Shan, and the age when the strain was blocked within the strata. At time t1, the collision of the Indian and Asian plates was initiated, and the tectonic strain instantaneously caused the uplift of the Tibetan Plateau. Subsequently, the tectonic strain passed to the northeastern margin of the Tibetan Plateau during $\triangle t$, though a series of geological formations (Figure 11a). At time t2, the strain reached the Liupan Shan; the mountains were uplifted and the strain was blocked within the strata in a very short time (t2+$\triangle t$, $\triangle t$ can be ignored in the context to the long geologic time; Figure 11b). Therefore, the timing of the increased strain derived from the AMS records should be closer to the timing of the uplift of the Liupan Shan but later than that of the uplift of the Tibetan Plateau.

In addition to its northeastern edge, the entire Tibetan Plateau experienced major tectonic activity during the Miocene (Coleman & Hodges, 1994; Harrsion et al., 1992; Lu et al., 2016; Sobel & Dumitru, 1997; Sun et al., 2005), as indicated by the following lines of evidence. (The distribution of the study sites is

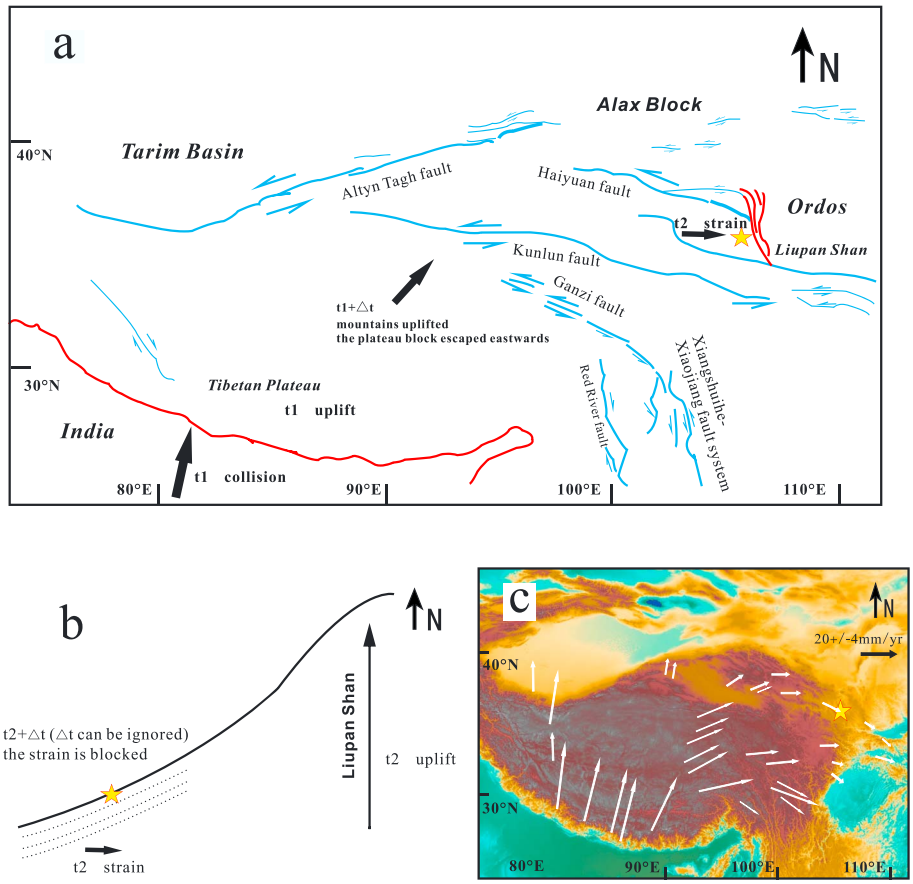


**Figure 11.** Conceptual model shows the timing differences in the uplift of the Tibetan Plateau, the Liupan Shan, and the strain locked within the strata of the studied section. The yellow star is the study site. (a) Process of compression by Indian Plate passing to the northeastern margin of the Tibetan Plateau. (b) Relationship between the uplift of the Liupan Shan and the strain locked within the strata. (c) Global Positioning System (GPS) velocity vectors with respect to stable Eurasia, plotted on a Digital elevation map of Asia compiled from Wang et al. (2001). At time t1, the collision of the Indian and Asian plates caused the instantaneous uplift of the Tibetan Plateau. Subsequently, by $\triangle t$, the strain was transmitted to the northeastern margin of the Tibetan Plateau. At time t2, the strain reached the Liupan Shan, the mountain was uplifted, and the strain was blocked within the strata.

shown in Figure 1a.): (1) Qilian Shan and Kunlun Shan: AFT and vitrinite-reflectance data confirm that the northern Qilian Shan experienced rapid uplift from 20 to 10 Myr (George et al., 2001), as did the Kunlun Shan (Yuan et al., 2006). (2) Tian Shan: Hendrix et al. (1994) concluded that the rapid uplift of the Tian Shan began at the Oligocene-Miocene boundary, based on AFT dating (Hendrix et al., 1994; Sobel & Dumitru, 1997). (3) Southern Tibet: Combining the work of Harrsion et al. (1992) in southern Tibet with that of Spicer et al. (2003), it can be concluded that rapid uplift occurred during 20–15 Myr. (4) Guide Basin: Bio-magnetostratigraphic studies of the Neogene sedimentary strata show that the Guide Basin experienced clockwise rotation caused by the collision of Indian and Asian plates during the middle Miocene (Yan et al., 2006). In addition, magnetostratigraphy, sedimentology and $^{40}Ar/^{39}Ar$ dating showed that the uplift of the northern edge of the Tibetan Plateau occurred during the Miocene (Coleman & Hodges, 1994; Lu, Li, & Liu, 2014; Sun et al., 2005). The occurrence of tectonic activity throughout the Tibetan Plateau on early-middle Miocene indicates that this interval was critical for the construction of the plateau.

## 6. Conclusions

Our magnetostratigraphic results show that the Kaimengou red clay section spans the interval from 19.8 to 12.8 Myr. The AMS results for the sequence show that the region was persistently under strain in an E-W

direction during this period and that the strain increased significantly during 19.5–18.5 Myr and 15.5–14.0 Myr. We attribute the strain to the far-field influence of the collision of the Indian and Asian plates. The far-field influence of the collision of the Indian and Asian plates reached the Liupan Shan area, which resulted in mountain building during the early-middle Miocene.

A substantial amount of research has focused on the uplift of the Liupan Shan, but by the difference in the timing precision and the sensitivity in tracing tectonic strain, the timing of the uplift remains controversial. Our results provide robust evidence for the timing of the uplift of the Liupan Shan and the Tibetan Plateau, and they increase our understanding of the tectonic consequences of the collision of the Indian and Asian plates. In addition, we find that the AMS can be used to trace tectonic strain in the red clay. And much additional research in other area needs to be done to validate it in the future research.

**Acknowledgments**
This work is supported by the "Strategic Priority Research Program" of the Chinese Academy of Sciences (grants XDB26020401 and XDA19050104), the National Key R&D Program of China (grant 2017YFA0603404), and the National Natural Science Foundation of China (grant 41272206). Digital elevation map (Figure 1a and 11c) is downloadable from https://www.gebco.net/data_and_products/gridded_bathymetry_data/. The magnetostratigraphy and bulk magnetic susceptibility of the Qin'an section are provide by Guo et al. (2002). The anisotropy of magnetic susceptibility data is provided in Supplemental Material S1, and the magnetostratigraphic data are provided in Supplemental Material S3 in the supporting information. We thank Haijian Lu for insightful discussion and Jan Bloemendal for improving an early version of the manuscript.

## References

Antoine, P., Goval, E., Jamet, G., Coutard, S., Moine, O., Hérisson, D., et al. (2014). Les séquences loessiques pléistocène supérieur d'Havrincourt (Pas-de-Calais, France): stratigraphie, paléoenvironnements, géochronologie et occupations paléolithiques. *Quaternaire*, *25*(4), 321–368. https://doi.org/10.4000/quaternaire.7278

Ao, H., Roberts, A. P., Dekkers, M. J., Liu, X., Rohling, E. J., Shi, Z., et al. (2016). Late Miocene-Pliocene Asian monsoon intensification linked to Antarctic ice-sheet growth. *Earth and Planetary Science Letters*, *444*, 75–87. https://doi.org/10.1016/j.epsl.2016.03.028

Besse, J., & Courtillot, V. (2003). Correction to "Apparent and true polar wander and the geometry of the geomagnetic field over the last 200 Myr". *Journal of Geophysical Research*, *108*(B10). EPM 6–1–31. https://doi.org/10.1029/2003JB002684

Borradaile, G. J. (2001). Magnetic fabrics and petrofabrics: Their orientation distribution and anisotropies. *Journal of Structural Geology*, *23*(10), 1581–1596. https://doi.org/10.1016/S0191-8141(01)00019-0

Borradaile, G. J., & Henry, B. (1997). Tectonic applications of magnetic susceptibility and its anisotropy. *Earth Science Reviews*, *42*(1-2), 49–93. https://doi.org/10.1016/S0012-8252(96)00044-X

Burchfiel, B. C., Zhang, P., Wang, Y., Zhang, W., Song, F., Deng, Q., et al. (1991). Geology of the Haiyuan fault zone, Ningxia-Hui Autonomous region, China, and its relation to the evolution of the northeastern margin of the Tibetan Plateau. *Tectonics*, *10*, 1091–1110. https://doi.org/10.1029/90TC02685

Burmeister, K. C., Harrison, M. J., Marshak, S., Ferré, E. C., Bannister, R. A., & Kodama, K. P. (2009). Comparison of Fry strain ellipse and AMS ellipsoid trends to tectonic fabric trends in very low-strain sandstone of the Appala chian fold-thrust belt. *Journal of Structural Geology*, *31*, 1028–1038. https://doi.org/10.1016/j.jsg.2009.03.010

Cifelli, F., Mattei, M., Chadima, M., Lenser, S., & Hirt, A. M. (2009). The magnetic fabric in "undeformed clays": AMS and neutron texture analyses from the Rif Chain (Morocco). *Tectonophysics*, *466*, 79–88. https://doi.org/10.1016/j.tecto.2008.08.008

Cifelli, F., Mattei, M., Hirt, A. M., & Günther, A. (2004). The origin of tectonic fabrics in "undeformed" clays: The early stages of deformation in extensional sedimentary basins. *Geophysical Research Letters*, *31*, L09604. https://doi.org/10.1029/2004GL019609

Coleman, M., & Hodges, K. (1994). Evidence for Tibetan plateau uplift before 14 Myr ago from a new minimum age for east-west extension. *Nature*, *374*(6517), 49–52. https://doi.org/10.1038/374049a0

Deng, C. (2008). Paleomagnetic and mineral magnetic investigation of the Baicaoyuan loess-paleosol sequence of the western Chinese Loess Plateau over the last glacial-interglacial cycle and its geological implications. *Geochemistry, Geophysics, Geosystems*, *9*, Q0403. https://doi.org/10.1029/2007GC001928

Deng, C., Shaw, J., Liu, Q., Pan, Y., & Zhu, R. (2006). Mineral magnetic variation of the Jingbian loess/paleosol sequence in the Northern Loess Plateau of China: Implications for Quaternary development of Asian aridification and cooling. *Earth and Planetary Science Letters*, *241*(1-2), 248–259.https://doi.org/10.1016/j.epsl.2005.10.020

Deng, C., Zhu, R., & Yuan, B. (2002). Rock magnetism of the Holocene eolian deposits in the Loess Plateau: Evidence for pedogenesis (in Chinese). *Marine Geology & Quaternary Geology*, *22*(4), 37–45. https://doi.org/10.16562/j.cnki.0256-1492.2002.04.006

Deng, T., Qiu, Z., Wang, B., & Hou, S. (2013). Late Cenozoic biostratigraphy of the Linxia Basin, northwestern China. In X. M. Wang, L. J. Flynn, & M. Fortelius (Eds.), *Fossil mammals of Asia: Neogene biostratigraphy and chronology* (pp. 243–273). New York: Columbia University Press. https://doi.org/10.7312/columbia/9780231150125.003.0009

Ding, G., Chen, J., Tian, Q., Shen, X., Xing, C., & Wei, K. (2004). Active faults and magnitudes of left-lateral displacement along the northern margin of the Tibetan Plateau. *Tectonophysics*, *380*(3-4), 243–260. https://doi.org/10.1016/j.tecto.2003.09.022

Dunlop, D. J., & Ozdemir, O. (2001). *Rock magnetism: Fundamentals and frontiers*, (p. 596). Cambridge, U. K: Cambridge University. Press.

Fang, X., Lv, L., Yang, S., Li, J., An, Z., Jiang, P., & Cheng, X. (2002). Loess in Kunlun Mountains and its implications on desert development and Tibetan Plateau uplift in west China. *Science in China (Series D)*, *45*(4), 289–299. https://link.springer.com/article/10.1360/02yd9031

Gao, F., Wang, Y., Liu, S., & Hu, B. (2000). Thermal history study in the west of the ordos basin using apatite fission track analysis (in Chinese). *Geotectonica et Metallog enia*, *24*(1), 87–91. https://doi.org/10.16539/j.ddgzyckx.2000.01.014

Gao, R., Wang, H., Yin, A., Dong, S., Kuang, Z., Zuza, A. V., et al. (2013). Tectonic development of the northeastern Tibetan Plateau as constrained by high-resolution deep seismic-reflection data. *Lithosphere*, *5*(6), 555–574. https://doi.org/10.1130/L293.1

Gao, X., Qiang, X., Zhao, H., & Chen, T. (2014). Anisotropy of magnetic susceptibility response to the regional stress variation in aeolian red clay sequence (in Chinese). *Advances in Earth Science*, *3*, 369–379. https://doi.org/10.11867/j.issn.1001-8166.2014.03.0369

García-Lasanta, C., Oliva-Urcia, B., Casas-Sainz, A. M., Román-Berdiel, T., Izquierdo-Llavallc, E., Soto, R., et al. (2018). Inversion tectonics and magnetic fabrics in Mesozoic basins of the Western Tethys: A review. *Tectonophysics*, *745*, 1–23. https://doi.org/10.1016/j.tecto.2018.08.005

García-Lasantaa, C., Oliva-Urciab, B., Román-Berdiela, T., Antonio, M., Casas, A. M., & Perez-Lorente, F. (2013). Development of magnetic fabric in sedimentary rocks: insights from early compactional structures. *Geophysical Journal International*, *194*(1), 182–199. https://doi.org/10.1093/gji/ggt098

Gaudemer, Y., Tapponnier, P., Meyer, B., Peltzer, G., Shunmin, G., Zhitai, C., et al. (1995). Partitioning of crustal slip between linked, active faults in the eastern Qilian Shan, and evidence for a major seismic gap, the 'Tianzhu gap,' on the western Haiyuan fault, Gansu (China). *Geophysical Journal International*, *120*(3), 599–645. https://doi.org/10.1111/j.1365-246X.1995.tb01842.x

Ge, J., Guo, Z., Zhao, D., Zhang, Y., Wang, T., Yi, L., & Deng, L. (2014). Spatial variations in paleowind direction during the last glacial period in North China reconstructed from variations in the anisotropy of magnetic susceptibility of loess deposits. *Tectonophysics*, *629*, 353–361. https://doi.org/10.1016/j.tecto.2014.07.002

George, A. D., Marshallsea, S. J., Wyrwoll, K.-H., Chen, J., & Lu, Y. (2001). Miocene cooling in the northern Qilian Shan, northeastern margin of the Tibetan plateau, revealed by apatite fission-track and vitrinitereflectance analysis. *Geology*, *29*, 939–942. https://doi.org/10.1130/0091-7613(2001)029<0939:MCITNQ>2.0.CO;2

Gong, H., Zhang, R., Yue, L., Zhang, Y., & Li, J. (2015). Magnetic fabric from Red clay sediments in the Chinese Loess Plateau. *Scientific Reports*, *5*(1), 1–6. https://doi.org/10.1038/srep09706

Guo, Z., Ruddiman, W. F., Hao, Q., Wu, H., Qiao, Y., Zhu, R., et al. (2002). Onset of Asian desertification by 22 Myr ago inferred from loess deposits in China. *Nature*, *416*(6877), 159–163. https://doi.org/10.1038/416159a

Harrsion, T. M., Copeland, P., & Kidd, W. S. F. (1992). Raising Tibet. *Science*, *255*(5052), 1663–1670.https://doi.org/10.1126/science.255.5052.1663

Hendrix, M. S., Dumitru, T. A., & Graham, S. A. (1994). Late Oligocene-early Miocene unroofing in the Chinese Tian Shan: An early effect of the India-Asia collision. *Geology*, *22*(6), 487–490. https://doi.org/10.1130/0091-7613(1994)022<0487:LOEMUI>2.3.CO;2.

Hrouda, F., & Kahan, S. (1991). The magnetic fabric relationship between sedimentary and basement nappes in the High Tatra Mountains, N. Slovakia. *Journal of Structural Geology*, *13*(4), 431–442. https://doi.org/10.1016/0191-8141(91)90016-C

Huang, B., John, D. A., Peng, S., Liu, T., Li, Z., Wang, Q., & Zhu, R. (2006). Magnetostratigraphic study of the Kuche Depression, Tarim Basin, and Cenozoic uplift of the Tian Shan Range, Western China. *Earth and Planetary Science Letters*, *251*(3-4), 346–364. https://doi.org/10.1016/j.epsl.2006.09.020

Kirschvink, J. (1980). The least-squares line and plane and the analysisi of palaeomagenetic data. *Geophysical Journal International*, *62*, 699–718. https://doi.org/10.1111/j.1365-246X.1980.tb02601.x

Lagroix, F., & Banerjee, S. K. (2002). Paleowind directions from the magnetic fabric of loess profiles in central Alaska. *Earth and Planetary Science Letters*, *195*, 99–112. https://doi.org/10.1016/S0012-821X(01)00564-7

Lagroix, F., & Banerjee, S. K. (2004). The regional and temporal significance of primary aeolian magnetic fabrics preserved in Alaskan loess. *Earth and Planetary Science Letters*, *225*, 379–395. https://doi.org/10.1016/j.epsl.2004.07.003

Larrasoaña, J. C., Gómez-Paccard, M., Giralt, S., & Roberts, A. P. (2011). Rapid locking of tectonic magnetic fabrics in weakly deformed mudrocks. *Tectonophysics*, *507*(1-4), 16–25. https://doi.org/10.1016/j.tecto.2011.05.003

Larrasoaña, J. C., Pueyo, E. L., & Parés, J. M. (2004). An integrated AMS, structural, palaeo-and rock-magnetic study of Eocene marine marls from the Jaca-Pamplona basin (Pyrenees, N Spain): New insights into the timing of magnetic fabric acquisition in weakly deformed mudrocks. *Geological Society of London, Special Publication*, *238*(1), 127–143. https://doi.org/10.1144/GSL.SP.2004.238.01.10

Li, J., Ma, Z., Li, X., Peng, T., Guo, B., Zhang, J., et al. (2017). Late Miocene-Pliocene geomorphological evolution of the Xiaoshuizi Peneplain in the Maxian Mountains and its tectonic significance for the northeastern Tibetan Plateau. *Geomorphology*, *295*, 393–405. https://doi.org/10.1016/j.geomorph.2017.07.024

Li, J., Yue, L., Pan, F., Zhang, R., Guo, L., Xi, R., & Guo, L. (2014). Intensified aridity of the Asian interior recorded by the magnetism of red clay in Altun Shan, NE Tibetan Plateau. *Palaeogeography, Palaeoclimatology, Palaeoecology*, *411*, 30–41. https://doi.org/10.1016/j.palaeo.2014.06.017

Li, S., Deng, C., Paterson, G. A., Yao, H., Huang, S., Liu, C., et al. (2014). Tectonic and sedimentary evolution of the late Miocene-Pleistocene Dali Basin in the southeast margin of the Tibetan Plateau: Evidences from anisotropy of magnetic susceptibility and rock magnetic data. *Tectonophysics*, *629*, 362–377. https://doi.org/10.1016/j.tecto.2014.05.035

Li, W., Dong, Y., Guo, A., Liu, X., & Zhou, D. (2013). Chronology and tectonic significance of Cenozoic faults in the Liupanshan Arcuate Tectonic Belt at the northeastern margin of the Qinghai-Tibet Plateau. *Journal of Asian Earth Sciences*, *73*, 103–113. https://doi.org/10.1016/j.jseaes.2013.04.026

Li, Y., Shan, X., Qu, C., & Wang, Z. (2016). Fault locking and slip rate deficit of the Haiyuan-Liupanshan fault zone in the northeastern margin of the Tibetan Plateau. *Journal of Geodynamics*, *102*, 47–57. https://doi.org/10.1016/j.jog.2016.07.005

Li, Y., Shan, X., Qu, C., Zhang, Y., Song, X., Jiang, Y., et al. (2017). Elastic block and strain modeling of GPS data around the Haiyuan-Liupanshan fault, northeastern Tibetan Plateau. *Journal of Asian Earth Sciences*, *150*, 87–97. https://doi.org/10.1016/j.jseaes.2017.10.010

Lin, X., Chen, H., Wyrwoll, K.-H., Batt, G. E., Liao, L., & Xiao, J. (2011). The uplift history of the Haiyuan-Liupan Shan Region Northeast of the Present Tibetan Plateau: Integrated constraint from stratigraphy and thermochronology. *The Journal of Geology*, *119*(4), 372–393. https://doi.org/10.1086/660190

Lin, X., Chen, H., Wyrwoll, K.-H., & Cheng, X. (2010). Commencing uplift of the Liupan Shan since 9.5 Ma: Evidences from the Sikouzi section at its east side. *Journal of Asian Earth Sciences*, *37*(4), 350–360. https://doi.org/10.1016/j.jseaes.2009.09.005

Liu, Y., Fang, X., Song, C., Li, L., & Cheng, Y. (2009). Cenozoic tectonic rotation of the Liupan Shan Region in the northeastern Tibetan Plateau and its implications (in Chinese). *Geotectonica et Metallogenia*, *33*(2), 189–198. https://doi.org/10.3969/j.issn.1001-1552.2009.02.001

Lu, H., Fu, B., Shi, P., Ma, Y., & Li, M. (2016). Constraints on the uplift mechanism of northern Tibet. *Earth and Planetary Science Letters*, *453*, 108–118. https://doi.org/10.1016/j.epsl.2016.08.010

Lu, H., Li, H., & Liu, D. (2014). Uplift-driven climatic aridity during the Miocene: A case study of the Janggalsay Section, Southeast Tarim Basin (in Chinese). *Geology in China*, *41*(5), 1724–1734. https://doi.org/10.3969/j.issn.1000-3657.2014.05.026

Lu, H., Wang, E., & Meng, N. K. (2014). Paleomagnetism and anisotropy of magnetic susceptibility of the Tertiary Janggalsay section (southeast Tarim basin): Implications for Miocene tectonic evolution of the Altyn Tagh Range. *Tectonophysics*, *618*, 67–78. https://doi.org/10.1016/j.tecto.2014.01.031

Maffione, M., Fernandez-Moreno, C., Ghiglione, M., Speranza, F., van Hinsbergen, D. J. J., & Lodolo, E. (2015). Constraints on deformation of the Southern Andes since the Cretaceous from anisotropy of magnetic susceptibility. *Tectonophysics*, *665*, 236–250. https://doi.org/10.1016/j.tecto.2015.10.008

McFadden, P. L., & McElhinny, M. W. (1990). Classification of the reversal test in aleomagnetism. *Geophysical Journal International*, *103*(3), 725–729. https://doi.org/10.1111/j.1365-246X.1990.tb05683.x

Mulch, A., & Chamberlain, C. P. (2006). The rise and growth of Tibet. *Nature*, *439*, 670–671. http://lib.gig.ac.cn/local/nature/439,670-671.pdf

Ogg, J. G., Ogg, G. M., & Gradstein, F. M. (2016). *A Concise geologic time scale*. Cambridge, U. K: Cambridge University. Press.

Parés, J. M. (2004). How deformed are weakly deformed mudrocks? Insights from magnetic anisotropy. *Agu Full Meeting Abstracts*, *238*(1), 191–203. https://doi.org/10.1144/GSL.SP.2004.238.01.13

Parés, J. M., van der Pluijm, B. A., & Dinarès-Turell, J. (1999). Evolution of magnetic fabrics during incipient deformation of mudrocks (Pyrenees, Northern Spain). *Tectonophysics*, *307*(1), 1–14. https://doi.org/10.1016/S0040-1951(99)00115-8

Qiang, X., An, Z., Song, Y., Chang, H., Sun, Y., Liu, W., et al. (2011). New Eolian red clay sequence on the western Chinese Loess Plateau linked to onset of Asian desertification about 25 Ma ago. *Science in China (series D)*, *54*(1), 136–144. https://doi.org/10.1007/s11430-010-4126-5

Shen, X., Tian, Q., Ding, G., Wei, K., & Chen, Z. (2001). The Late Cenozoic stratigraphic sequence and its implication to tectonic evolution, Hejiakouzi Area, Ningxia Hui Autonomous Region (in Chinese). *Earthquake Research in China*, *17*(2), 156–166. https://doi.org/10.3969/j.issn.1001-4683.2001.02.006

Shi, W., Zhang, Y., & Ma, Y. (2006). Elevation distribution pattern of red clay beds in the regions east and west of Liupanshan and neotectonic significance (in Chinese). *Marine Geology & Quaternary Geology*, *26*(5), 123–130. https://doi.org/10.16562/j.cnki.0256-1492.2006.05.016

Sobel, E. R., & Dumitru, T. A. (1997). Thrusting and exhumation around the margins of the western Tarim basin during the India-Asia collision. *Journal of Geophysical Research*, *102*, 5043–5063. https://doi.org/10.1029/96JB03267

Song, Y., Fang, X., Dong, H., Qiang, X., Chang, H., Fu, C., & Fu, K. (2005). Geochronological and stratigraphical evidences for the uplift of the Liupan Shan, Northeastern boundary of the Tibetan Plateau. *International Geoscience and Remote Sensing Symposium*, *44*(7), 5223–5226. https://doi.org/10.1109/IGARSS.2005.1526862

Song, Y., Fang, X., Li, J., An, Z., & Miao, X. (2001). The Late Cenozoic uplift of the Liupan Shan, China. *Science in China Series D: Earth Sciences*, *44*, 176–184. https://doi.org/10.1007/BF02911985

Song, Y., Fang, X., Li, J., An, Z., & Yang, D. (2001). Age of red clay at Chaona section near eastern Liupan Mountain and its tectonic significance (in Chinese). *Quaternary Sciences*, *20*(5), 457–463. https://doi.org/10.3321/j.issn:1001-7410.2000.05.006

Soto, R., Larrasoaña, J. C., Arlegui, L. E., Beamud, E., Oliva-Urcia, B., & Simón, J. L. (2009). Reliability of magnetic fabric of weakly deformed mudrocks as a palaeostress indicator in compressive settings. *Journal of Structural Geology*, *31*, 512–522. https://doi.org/10.1016/j.jsg.2009.03.006

Spicer, R. A., Harris, N. B. W., Widdowson, M., Herman, A. B., Guo, S., Valdes, P. J., et al. (2003). Constant elevation of southern Tibet over the past 15 million years. *Nature*, *421*, 622–624. https://doi.org/10.1038/nature01356

Sun, D., Zhang, Y., Han, F., Zhang, Y., Yi, Z., Li, Z., et al. (2011). Magnetostratigraphy and palaeoenvironmental records for a Late Cenozoic sedimentary sequence from Lanzhou, Northeastern margin of the Tibetan Plateau. *Global and Planetary Change*, *76*(3-4), 106–116. https://doi.org/10.1016/j.gloplacha.2010.12.006

Sun, J., Ye, J., Wu, W., Ni, X., Bi, S., Zhang, Z., et al. (2010). Late Oligocece-Miocene mid-latitude aridification and wind patterns in the Asian interior. *Geology*, *38*(6), 515–518. https://doi.org/10.1130/G30776.1

Sun, J., Zhu, R., & An, Z. (2005). Tectonic uplift in the northern Tibetan Plateau since 13.7 Ma ago inferred from molasse deposits along the Altyn Tagh Fault. *Earth and Planetary Science Letters*, *235*, 641–653. https://doi.org/10.1016/j.epsl.2005.04.034

Tang, Z., Dong, X., Wang, X., & Ding, Z. (2015). Oligocene–Miocene magnetostratigraphy and magnetic anisotropy of the Baxbulak section from the Pamir–Tian Shan convergence zone. *Geochemistry Geophysics Geosystems*, *16*, 3575–3592. https://doi.org/10.1002/2015GC005965

Tang, Z., Huang, B., Dong, X., Ji, J., & Ding, Z. (2012). Anisotropy of magnetic susceptibility of the Jingou River section: Implications for late Cenozoic uplift of the Tian Shan. *Geochemistry Geophysics Geosystems*, *13*(1), 1525–2027. https://doi.org/10.1029/2011GC003966

Tapponnier, P., & Molnar, P. (1976). Slip-line field theory and large-scale continental tectonics. *Nature*, *264*(5584), 319. https://doi.org/10.1038/264319a0–324

Tapponnier, P., Xu, Z., Roger, E., Meyer, B., Arnaud, N., Wittlinger, G., & Yang, J. (2001). Oblique stepwise rise and growth of the Tibetan Plateau. *Science*, *294*(5547), 1671–1677. https://doi.org/10.1126/science.105978

Tauxe, L., Butler, R. F., Banerjee, S. K., & Van der Voo, R. (2010). *Essentials of paleomagnetism*, (p. 512). Berkeley: University of California Press.

Taylor, M., & Yin, A. (2009). Active structures of the Himalayan-Tibetan orogen and their relationships to earthquake distribution, contemporary strain field, and Cenozoic volcanism. *Geosphere*, *5*(3), 199–214. https://doi.org/10.1130/GES00217.1

Taylor, S. N., & Lagroix, F. (2015). Magnetic anisotropy reveals the depositional and postdepositional history of a loess-paleosol sequence at Nussloch (Germany). *Journal of Geophysical Research: Solid Earth*, *120*, 2859–2876. https://doi.org/10.1002/2014JB011803

Thistlewood, L., & Sun, J. (1991). A paleomagnetic and mineralmagnetic study of the loess sequence at Liujiapo, Xi'an, China. *Journal of Quaternary Science*, *6*, 13–26. https://doi.org/10.1002/jqs.3390060104

Wang, Q., Zhang, P., Freymueller, J. T., Bilham, R., Larson, K. M., Lai, X., et al. (2001). Present-day crustal deformation in China constrained by global positioning system measurements. *Science*, *294*(5542), 574–577. https://doi.org/10.1126/science.1063647

Xiong, J., Li, Y., Zhong, Y., Si, S., Lei, J., Xin, W., et al. (2017). Paleomagnetic age of the Tangxian planation surface, northwestern Zhongtiao Shan of the Shanxi Graben System, North China. *Geomorphology*, *283*, 17–31. https://doi.org/10.1016/j.geomorph.2017.01.020

Yan, M., Van der Voo, R., Fang, X., Pares, J. M., & Rea, D. K. (2006). Paleomagnetic evidence for a mid-Miocene clockwise rotation of about 25 degrees of the Guide Basin area in NE Tibet. *Earth and Planetary Science Letters*, *241*(1-2), 234–247. https://doi.org/10.1016/j.epsl.2005.10.013

Yang, D., Fang, X., Song, Y., Lv, L., Li, J., & An, Z. (2002). Pediment near the Western Liupan Mountain and Its Implication on the Neotectonic Uplift (in Chinese). *Acta Sedimentologica Sinica*, *2*, 282–287. https://doi.org/10.3969/j.issn.1000-0550.2002.02.016

Yin, A., Dang, Y. Q., Wang, L. C., Jiang, W. M., Zhou, S. P., Chen, X. H., et al. (2008). Cenozoic tectonic evolution of Qaidam basin and its surrounding regions (Part 1): The southern Qilian Shan–Nan Shan thrust belt and northern Qaidam basin. *Geological Society of America Bulletin*, *120*, 813–846. https://doi.org/10.1130/b26180.1

Yuan, W., Carter, A., Dong, J., Bao, Z., An, Y., & Guo, Z. (2006). Mesozoic-Tertiary exhumation history of the Altaï Mountains, northern Xinjiang, China: Constraints from apatite fission track data. *Tectonophysics*, *412*, 183–193. https://doi.org/10.1016/j.tecto.2005.09.007

Zhang, P., Burchfiel, B. C., Molnar, P., Zhang, W., Jiao, D., Deng, Q., et al. (1991). Amount and style of Late Cenozoic Deformation in the Liupan Shan Area, Ningxia Autonomous Region, China. *Tectonics*, *10*, 1111–1129. https://doi.org/10.1029/90TC02686

Zhang, P., Zheng, D., Yin, G., Yuan, D., Zhang, G., Li, C., & Wang, Z. (2006). Discussion on Late Cenozoic growth and rise of northeastern margin of the Tibetan Plateau (in Chinese). *Quaternary Sciences*, *26*, 5–13. https://doi.org/10.3321/j.issn:1001-7410.2006.01.002

Zhang, R., Kravchinsky, V. A., Zhu, R., & Yue, L. (2010). Paleomonsoon route reconstruction along a W–E transect in the Chinese Loess Plateau using the anisotropy of magnetic susceptibility: Summer monsoon model. *Earth and Planetary Science Letters*, *299*(3-4), 436–446. https://doi.org/10.1016/j.epsl.2010.09.026

Zhang, Y., Xiong, S., Ding, Z., Lu, H., & Jiang, W. (2011). Carbon-oxygen isotope records of pedogenic carbonate from the Early Miocene–Pleistocene loess–red clay in the vicinity of the Liupanshan region and its implications for the early origin of C4 plants in the Chinese Loess Plateau. *Quaternary Sciences*, *31*(5), 800–811. https://doi.org/10.3969/j.issn.1001-7410.2011.05.05

Zhao, H., Sun, Y., & Qiang, X. (2017). Iron oxide characteristics of mid-Miocene Red Clay deposits on the western Chinese Loess Plateau and their paleoclimatic implications. *Palaeogeography Palaeoclimatology Palaeoecology*, *468*, 162–172. https://doi.org/10.1016/j.palaeo.2016.12.008

Zheng, D., Zhang, P., Wan, J., Yuan, D., Li, C., Yin, G., et al. (2006). Rapid exhumation at ~8 Ma on the Liupan Shan thrust fault from apatite fission-track thermochronology: Implications for growth of the northeastern Tibetan Plateau margin. *Earth and Planetary Science Letters*, *248*(1-2), 198–208. https://doi.org/10.1016/j.epsl.2006.05.023

Zijderveld, J. D. A. (1967). AC demagnetization of rocks: Analysis of results. *Methods in Paleomagnetism*, *3*, 254–286.

Zuza, A. V., Cheng, X. G., & Yin, A. (2016). Testing models of Tibetan Plateau formation with Cenozoic shortening estimates across the Qilian Shan–Nan Shan thrust belt. *Geosphere*, *12*(2), 501–532. https://doi.org/10.1130/GES01254.1